Final Technical Report

ONR Grant #N00014-04-1-0237
Performance Period: 1 December 2003 – 30 September 2008

I. Lagrangian Observations of Nonlinear Internal Waves and Turbulence Mixing in Luzon Strait and South China Sea
&
II. Internal Wave in the Vicinity of the Kuroshio Path

Ren-Chieh Lien
Applied Physics Laboratory, University of Washington, Seattle, Washington 98105
phone: (206) 685-1079 fax: (206) 543-6785 email: lien@apl.washington.edu

Eric A. D'Asaro
Applied Physics Laboratory, University of Washington, Seattle, Washington 98105
phone: (206) 685-2982 fax: (206) 543-6785 email: dasaro@apl.washington.edu

OVERVIEW

Two projects were supported by this award. In the following, we separately report objectives, approaches, work completed, results, and publications.

I. LAGRANGIAN OBSERVATIONS OF NONLINEAR INTERNAL WAVES AND TURBULENCE MIXING IN LUZON STRAIT AND SOUTH CHINA SEA

OBJECTIVES

The primary objectives of this project were 1) to identify the generation site and understand the generation mechanism of nonlinear internal waves, 2) to understand the evolution of nonlinear internal waves interacting with abrupt topography, and 3) to quantify the energy budget and energy cascade from internal tides to nonlinear internal waves near DongSha Island in the northern South China Sea. Our particular interest was to understand the energy cascade from barotropic tides, internal tides, nonlinear internal waves, to turbulence mixing in the northern South China Sea.

APPROACH

Our approach was to conduct an observational experiment near DongSha Island in collaboration with Taiwanese investigators. The primary instrument was the Lagrangian float. The float is designed to accurately follow water motions at high frequencies through a combination of matching the density of seawater and using a high drag provided by a cloth drogue. Lagrangian floats are particularly effective at measuring vertical velocity. High-frequency internal waves,

REPORT DOCUMENTATION PAGE

Form Approved
OMB No. 0704-0188

1. REPORT DATE *(DD-MM-YYYY)*	2. REPORT TYPE	3. DATES COVERED *(From - To)*
30/12/2008	Final Performance Technical Report	December 1, 2003-September 30, 2008

4. TITLE AND SUBTITLE

Lagrangian Observations of Nonlinear Internal Waves and Turbulence Mixing in Luzon Strait and South China Sea,

and

Internal Waves in the Vicinity of the Kuroshio Path

5a. CONTRACT NUMBER

5b. GRANT NUMBER
N00014-04-1-0237

5c. PROGRAM ELEMENT NUMBER

6. AUTHOR(S)
Ren-Chieh Lien

5d. PROJECT NUMBER

5e. TASK NUMBER

5f. WORK UNIT NUMBER

7. PERFORMING ORGANIZATION NAME(S) AND ADDRESS(ES)
Applied Physics Laboratory, University of Washington
1013 N.E. 40th Street
Seattle, WA 98105

8. PERFORMING ORGANIZATION REPORT NUMBER

9. SPONSORING/MONITORING AGENCY NAME(S) AND ADDRESS(ES)
Theresa Paluszkiewicz, Code 32
Office of Naval Research
875 North Randolph Street
Arlington, VA 22203-1995

10. SPONSOR/MONITOR'S ACRONYM(S)

11. SPONSOR/MONITOR'S REPORT NUMBER(S)

12. DISTRIBUTION/AVAILABILITY STATEMENT
UU

13. SUPPLEMENTARY NOTES

14. ABSTRACT

Two related projects were funded sequentially under the same grant #. The first was to conduct an experiment near DongSha Island, using the Lagrangian float, to understand the energy cascade from barotropic tides, internal tides, nonlinear internal waves, to turbulence mixing in the northern South China Sea. Results are reported. The second was to analyze observations of data taken in the vicinity of the Kuroshio path from Luzon Strait to the southern East China Sea. Results are reported.

15. SUBJECT TERMS

16. SECURITY CLASSIFICATION OF:			17. LIMITATION OF ABSTRACT	18. NUMBER OF PAGES	19a. NAME OF RESPONSIBLE PERSON
a. REPORT	b. ABSTRACT	c. THIS PAGE			Ren-Chieh Lien
UU	UU	UU	UU	1	19b. TELEPHONE NUMBER *(Include area code)* 206-685-1079

e.g., nonlinear internal waves in the South China Sea, have a strong vertical velocity signal. These floats are also capable of measuring dissipation rates of turbulence kinetic energy ε from their acceleration spectra using an inertial subrange method. The Lagrangian acceleration spectrum is white within the inertial subrange with a level proportional to ε. For the meter-sized floats, the finite size of the float and the noise level of the float measurements set a lower limit of estimates of $\varepsilon > 10^{-8} W\ kg^{-1}$ under most oceanic conditions (Lien and D'Asaro, 2005).

WORK COMPLETED

A set of mooring ADCP data provided by Dr. David Tang of National Taiwan University was analyzed and results were published (Lien et al., 2005 and Chang et al., 2006). These ADCP records clearly showed strong and highly predictable nonlinear internal waves on the continental slope and shelf in the vicinity of DongSha Island.

In April 18-May 1 of 2005, we conducted an experiment near DongSha Island in the northern South China Sea (Fig. 1). We used (1) a Lagrangian-float to measure nonlinear internal waves and turbulence, and (2) the shipboard ADCP and CTD to capture properties of nonlinear internal waves. The surface signature of nonlinear internal waves was captured by the shipboard marine radar and satellite images. The scattering strength from EK500 provided the interior signature of nonlinear internal waves. Two papers were published (Moore and Lien 2007, Chang et al., 2008).

RESULTS

Our measurements were taken mostly along 21 N between 118 and 116.5 E on a plateau of about 350-500-m depth. Profiles of XCP-XCTD were taken by Dr. Hibiya on stations O and D for two days to measure internal tidal energy flux. During the neap tide in the first leg of experiment, three second-mode nonlinear internal waves were observed of amplitude about 20 m. During the spring tide in the second leg, large-amplitude nonlinear internal waves (LNIW) appeared on the plateau of the water depth of 350-500 m (Fig. 2). Amplitudes of nonlinear internal waves were recorded by the Lagrangian float and were estimated by examining the images of EK500. Large-amplitude nonlinear internal waves were all first-mode waves. Surface signatures of nonlinear internal waves were captured by the marine radar on OR3. The clear surface signature associated with the large-amplitude wave was discernible even with bared eyes.

During the spring tide the LNIW arrived approximately diurnally (Fig. 3) west of station E (Fig. 1), and was not detected east of the station E during our transits. The largest amplitude of nonlinear internal waves recorded by the float was 157 m (labeled in Fig. 3).

To capture the evolution of LNIW as they propagated across the plateau, we tracked the waves and made intensive measurements of CTD profiles, EK500, and shipboard ADCP along 21 N between stations E and D (Fig. 1). A salient feature of the evolution of LNIW was revealed (Figs. 4-6). At 117.5 E (near station E), the LNIW appeared as single depression wave with the maximum horizontal current of 2 m s^{-1} and the vertical current of 0.4 m s^{-1} (Fig. 4). At ~117 E (near station D), the LNIW had evolved into a wave train (Fig. 5). The leading wave was further developing into two waves with two cores of maximum horizontal velocity separated by a

vertical upwelling. The first core had a maximum horizontal current of ~1.2 m s^{-1} and the second core of ~0.9 m s^{-1}. The detailed density structure in the leading wave constructed using measurements taken by yoyo CTD profiles revealed overturning of the order of 50 m near the trough of the leading wave between the two cores of maximum horizontal currents. At 116.7 E (near station W), the LNIW has developed into a train of more than 3 waves. The maximum horizontal current in the leading wave is about 0.6 m s^{-1} and the vertical current is about 0.2 m s^{-1} (Fig. 6). There is no obvious overturning in the density field within the leading wave. Likely, the evolution of NLIWs into a wave train is a dissipative process. Another example of large vertical overturning of 75 m within the leading wave of a wave train was found again near station D (Fig. 7). Across the plateau, the LNIW evolved from a single wave into a train of many waves. The wave energy was dissipated rapidly when the waves propagated westward and the turbulence mixing was strong in the upper layer across the plateau.

The Lagrangian float encountered a single wave with an amplitude of 157 m and a vertical velocity of ~0.6 m s^{-1} (Fig. 8). It took about 13 minutes for the wave to pass the float. Before the wave arrived, the float was at 40-m depth, ~ 3 m below the depth of the peak value of the buoyancy frequency. After the wave passed, the float returned to the initial depth. However, the vertical impression of the wave captured by the float was not symmetric.

Inviscid, adiabatic, and steady internal waves of arbitrary amplitude in a horizontal homogeneous fluid can be described by the Dubreil-Jacotin-Long equation (or Long's equation) (D'Asaro et al., 2005), i.e.,

$$\nabla^2\xi + N_r^2(z-\xi)\xi / v^2 = 0,$$

where ξ is the vertical displacement, v is the wave speed, N_r^2 is the squared background buoyancy frequency, and $\nabla^2 = \partial_x^2 + \partial_z^2$.

The solution of the Long's equation of amplitude of 157 m is compared with the float's observation (Fig. 9). The wave speed of the Long's solution is 1.68 m s^{-1}. The vertical trajectory of the Lagrangian float agrees with the Long's solution only in the downwelling phase of the wave, but the float ascends about 100 s earlier than that of the Long's solution. The density field measured by the float shows that the density is constant (adiabatic) in the downwelling phase, and becomes lighter when the float approaches the trough of the wave. The density change is about 0.04 kg m^{-3}. In other words, the turbulence mixing occurs near the trough of the wave. The relation between the wave amplitude and δt, the time interval between the float passing the depths of half of the wave amplitude, observed by the float is compared with that of the Long's solutions (Fig. 9). The agreement between the float's observation and the Long's solution is fair. The discrepancy is presumably due to the presence of diapycnal mixing and the unsteadiness of the wave.

Measurements taken in this experiment were analyzed, supported by another ONR project. Two papers were published (Moore and Lien, 2007, Chang et al. 2008). These are briefly discussed as follows.

Bio-Physical Coupling: Pilot Whales Following NLIWs in SCS

Schools of pilot whales were observed behind the large-amplitude NLIWs. Moore and Lien (2007) proposed that prey availability for pilot whales in the SCS is influenced by the aggregative properties of NLIWs. This is the first report of cetaceans associated with internal waves. We expect that the ecosystem in the SCS is strongly modulated by properties of NLIWs.

Radar Detection of NLIW Properties

Surface waves are modulated by NLIWs. In SCS, the interaction is extremely strong due to the large horizontal velocity convergence of NLIWs (Chang et al., 2008). Photos taken during the experiment show a sequence of calm sea surface, breaking surface waves, isotropic surface waves, and boils during the passage of the NLIW during a calm day (Fig. 10). The shipboard marine radar reveals the strongest scattering strength corresponding to the strongest horizontal velocity convergence measured by the shipboard ADCP (Fig. 10b and 10c).

A composite view of the sea surface scattering strength, the horizontal velocity convergence and the vertical displacement of NLIWs is constructed (Fig. 11). The strongest surface scattering strength appears at the front portion of the NLIW, ~0.5 $\lambda_{\eta/2}$, where $\lambda_{\eta/2}$ is the wave-width at half of the maximum amplitude.

An empirical formula between the surface scattering strength and horizontal velocity convergence is obtained (Fig. 12). It shows a linear relation at low horizontal velocity convergence, and reaches an asymptotic value at high horizontal velocity convergence, indicating a saturation state presumably due to breaking surface waves. Following the power-law and the linear fits between the scattering strength and the local wind speed, the maximum surface scattering enhancement by NLIWs is equivalent to that caused by a wind of ~6 m s^{-1} with surface waves of ~1.5 m, according to the Beaufort wind scale. In other words, the surface scattering enhancement induced by NLIWs will be overwhelmed by that induced by the wind and can not be identified with the X-band radar when the wind is stronger than 6 m s^{-1}. The vertical displacement of NLIWs is found to be proportional to the spatial integration of the surface scattering strength (not shown). Our analysis concludes that in the low-wind condition remote sensing measurements may provide useful predictions of horizontal velocity convergences, amplitudes, and spatial structures of NLIWs. Further applications and modification of our empirical formulas in different conditions of wind speed, surface waves, and NLIWs, or with other remote sensing methods should be investigated.

PUBLICATIONS

Lien, R.-C., T. Y. Tang, M. H. Chang, E. A. D'Asaro, Energy of nonlinear internal waves in the South China Sea, *Geophys. Res. Lett.*, **32**, L05615, doi:10.1029/2004GL022012, 2005.

Chang, M.-H., R.-C. Lien, T. Y. Tang, E. A. D'Asaro, and Y. J. Yang, Energy flux of nonlinear internal waves in northern South China Sea, *Geophys. Res. Lett.*, **33**, L03607, doi:10.1029/2005GL025196, 2006.

Moore, S. E., and R.-C. Lien, Pilot whales follow internal solitary waves in the South China Sea, *Mar. Mamm. Sci.*, **23**, 1, 193–196, 2007.

Chang, M.-H., R.-C. Lien, T. Y. Tang, Y. J. Yang, and J. Wang, A Composite View of Surface Signatures and Interior Properties of Nonlinear Internal Waves: Observations and Applications., *J. Atmos. Ocean. Tech.*, **25**, 1218-1227, 2008.

REFERENCES

Chang, M-H, A study of internal solitons in the South China Sea, MS Thesis, National Taiwan University, 2001.

D'Asaro, E. A., R.-C. Lien, and F. Henyey, High frequency internal waves on the Oregon continental shelf, *J. Phys. Oceanogr.*, in press, 2005.

Lien, R.-C., T. Y. Tang, M. H. Chang, E. A. D'Asaro, Energy of nonlinear internal waves in the South China Sea, *Geophys. Res. Lett.*, **32**, L05615, doi:10.1029/2004GL022012, 2005.

Lien, R.-C., and E. A. D'Asaro, Measurement of turbulent kinetic energy dissipation rate with a Lagrangian float, *J. Atmos. Ocean. Technol.*, 2005, in press.

Zhao, Z., V. Klemas, Q. Zheng, and X.-H. Yang, Remote sensing evidence for baroclinic tide origin of internal solitary waves in the northeastern South China Sea, *Geophys. Res. Let.*, **31**, L06302, doi:10,1029/2003GL019077, 2004.

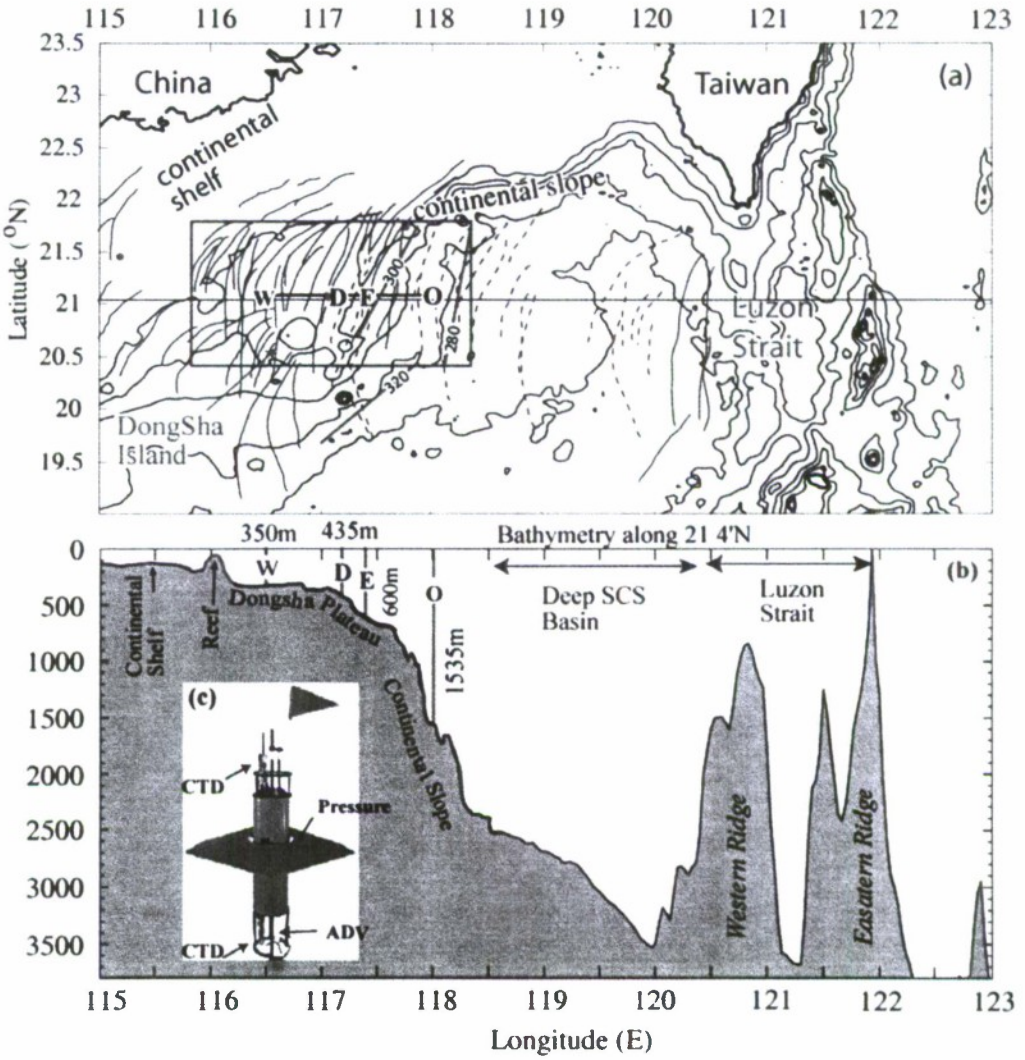

Figure 1: (a) Map of the northern South China Sea, and (b) bottom bathymetry along 21°4'N. In panel (a), green curves represent surface signatures of NLIWs identified in satellite images (Zhao et al., 2004), dashed for single-depression waves and solid for multiple wave packets. The blue box delineates the area where multiple wave packets are mostly found. Four primary stations in our April-May 2005 cruise are labeled as O, E, D and W. Shipboard and float measurements are taken along O-E-D-W. Three magenta curves illustrate isobaric orientations on the continental slope. In panel (b), two submarine ridges in the Luzon Strait are labeled. They are responsible for generating strong internal tides. Depths at four primary stations are also labeled. The inset (c) shows the Lagrangian float and sensors equipped on the float.

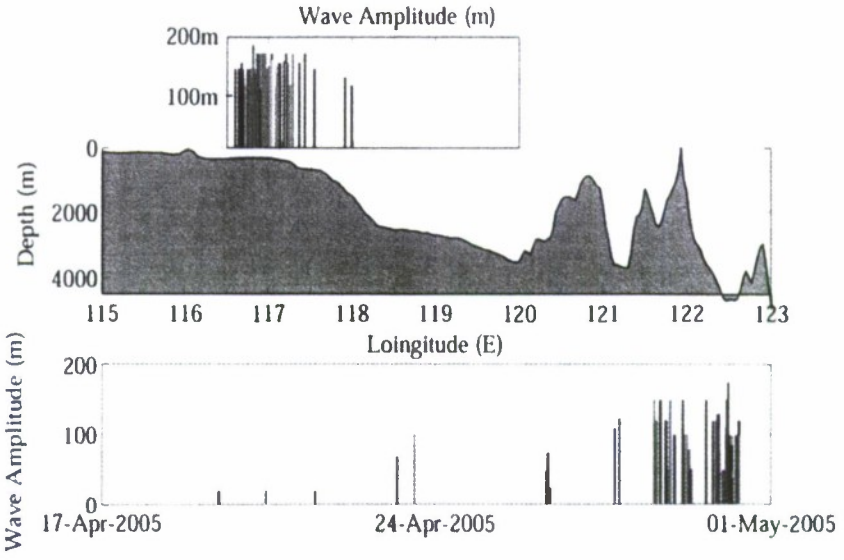

Figure 2. The top panel shows the geographical distribution of amplitudes of nonlinear internal waves observed by the Lagrangian float and the shipboard EK500. The bathymetry is shown in the middle panel. The bottom panel shows the time series of the observed wave amplitudes.

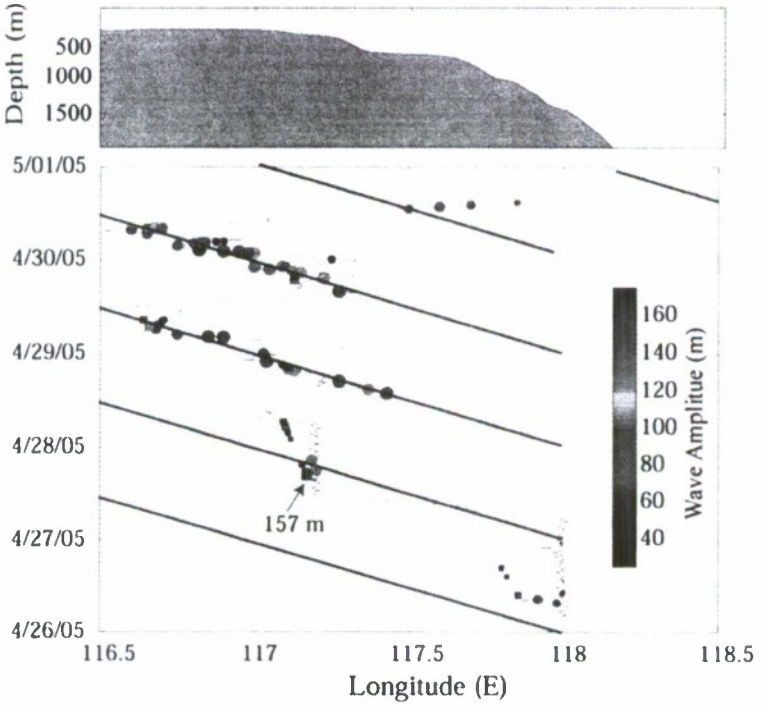

Figure 3. Summary of wave amplitudes as a function of longitude and time. Filled circles are waves detected by EK500 and filled squares are observed by the Lagrangian float. Colors and sizes represent the magnitude of the waves. The thin line shows the ship track. Magenta lines illustrate the diurnal arrival of large-amplitude nonlinear internal waves. A 157-m wave recorded by the Lagrangian float is labeled.

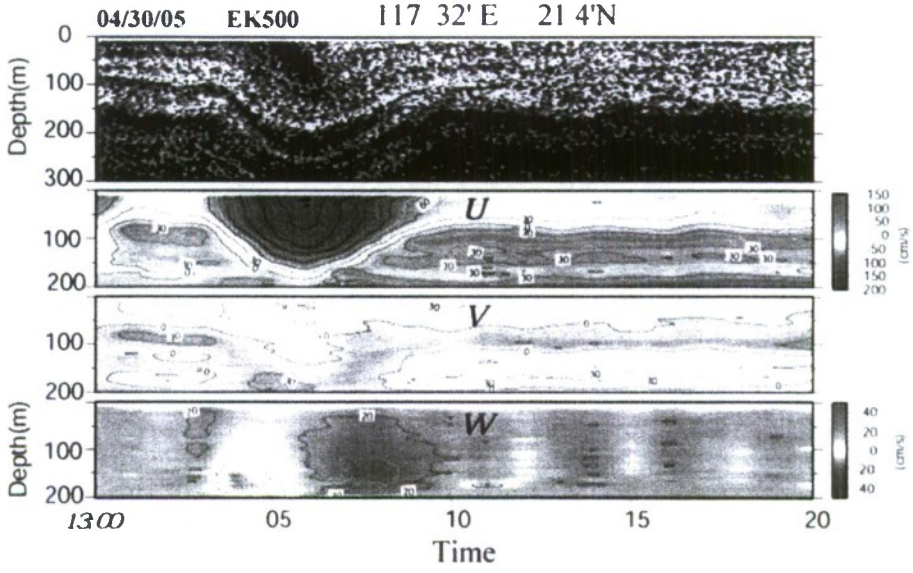

Figure 4. The EK500 image and contours of ADCP velocity components observed near station E.

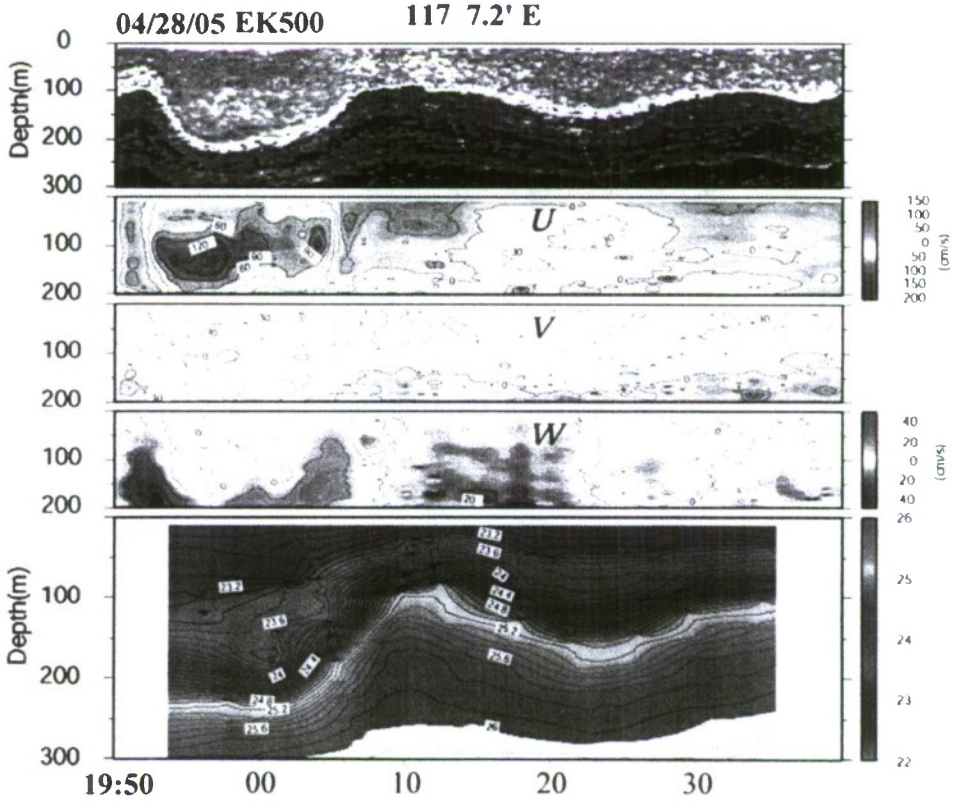

Figure 5. The EK500 image and contours of ADCP velocity observed near station D when the wave is developing into a wave train. The bottom panel shows the contour of density field.

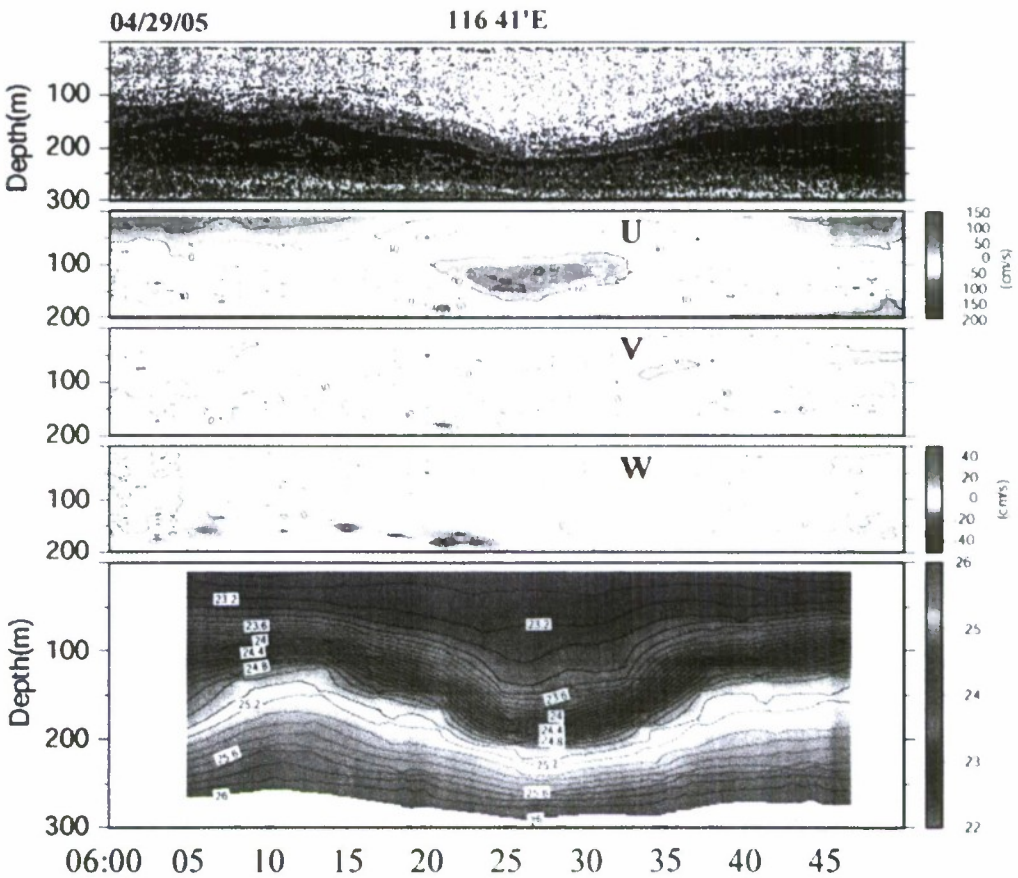

Figure 6. The EK500 image and contours of ADCP velocity of a leading wave within a wave train observed near station W. The bottom panel shows the density contour.

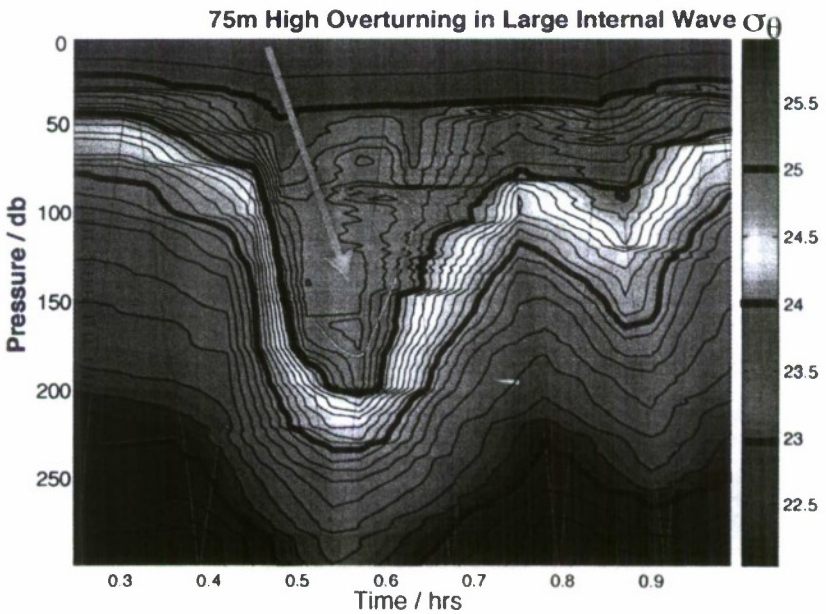

Figure 7. Contour of the density field of a train of waves. A large vertical overturning is present within the leading wave.

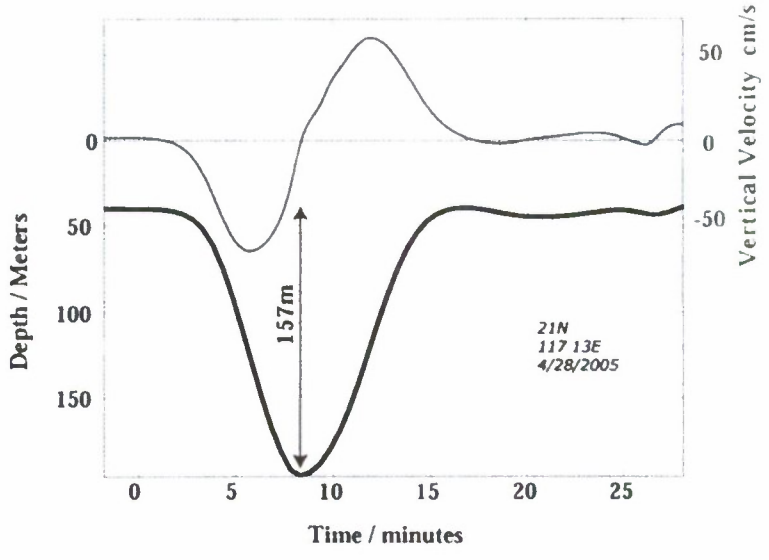

Figure 8. Vertical trajectory (black curve) and vertical velocity (red curve) of a nonlinear internal wave recorded by the Lagrangian float.

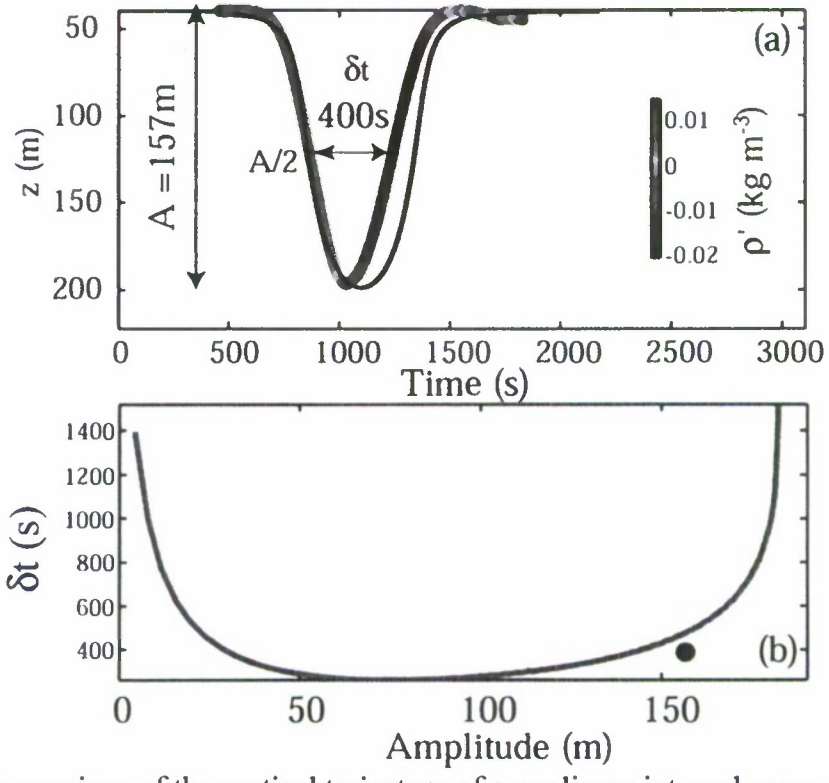

Figure 9. (a) Comparison of the vertical trajectory of a nonlinear internal wave captured by the Lagrangian float (colored curve) with the solution of the Long's equation (black curve), and (b) the time interval δt traveled by the float passing the depths of half of the wave amplitude (A/2) (blue dot) and that of Long's solution. The color shading in (a) represents the density anomaly measured by the Lagrangian float.

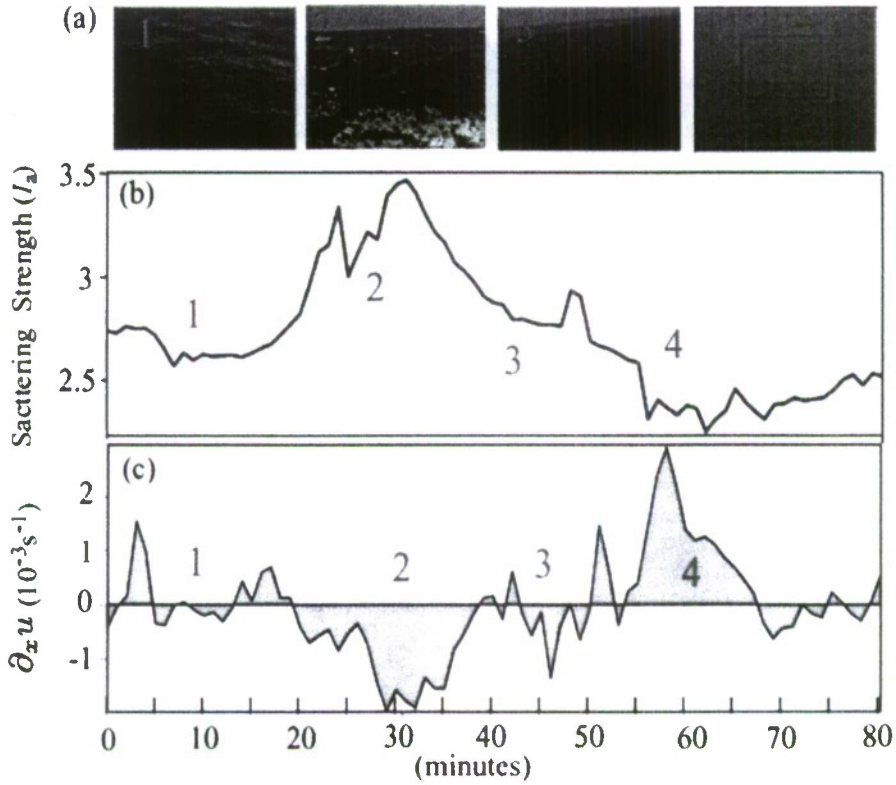

Figure 10: (a) Pictures taken during the experiment illustrating the surface signatures accompanying the passing NLIW, (b) the marine radar scattering strength, and (c) the horizontal velocity convergence computed from shipboard ADCP measurements in 8.4–12.4-m depth.

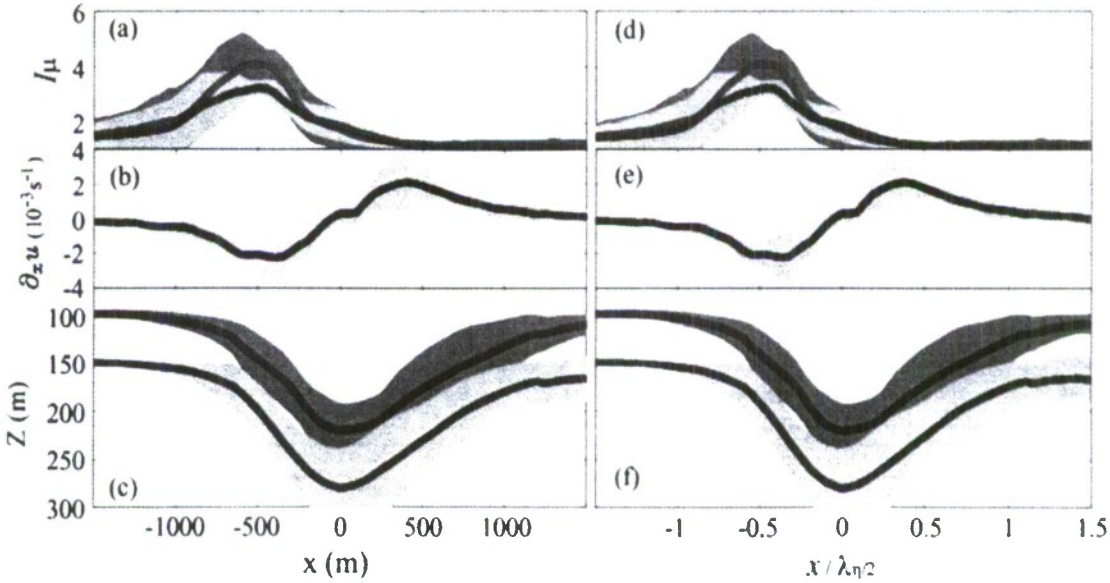

Figure 11: (a) Surface scattering strength, (b) horizontal velocity convergence, and (c) vertical displacement of NLIWs at initial depths of 100 and 150 m averaged over seven NLIW events. (d)–(f) are the same as (a)-(c) except that the x-axis is scaled by the wave width of the half

maximum amplitude. Red curves in (a) and (d) represent the surface scattering strength observed from ahead of the propagating NLIWs and the blue curves represent the surface scattering strength observed from behind the propagating NLIWs. The light gray and heavy gray shadings represent 95% confidence intervals.

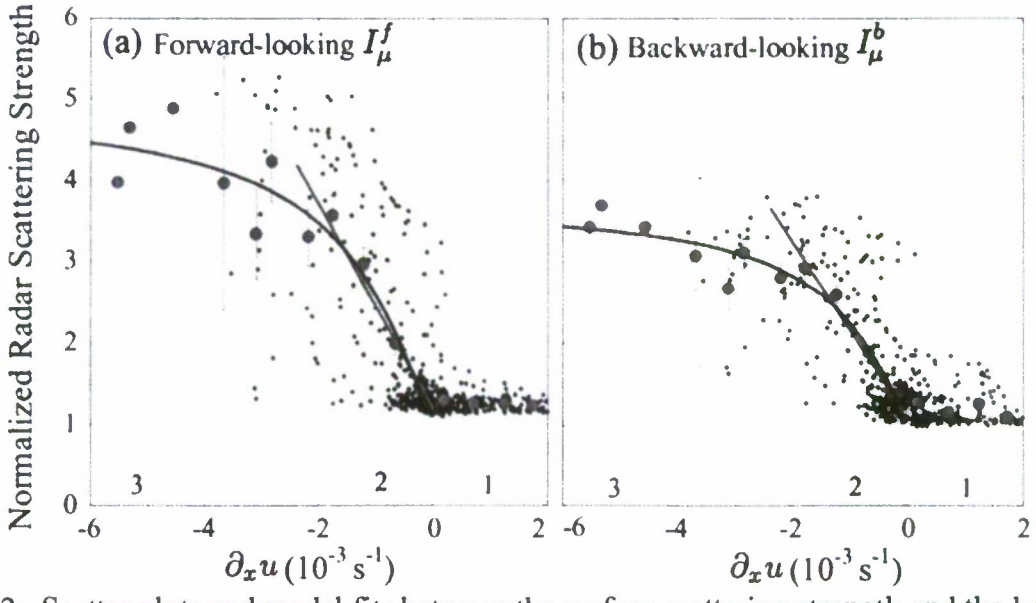

Figure 12: Scatter plots and model fits between the surface scattering strength and the horizontal velocity convergence computed from shipboard ADCP measurements. (a) Observations (gray dots) taken ahead of the propagating NLIWs. Red dots represent averages over constant intervals of horizontal convergence 0.005 s^{-1}. Vertical lines represent 95% confidence intervals. Red and blue curves represent the linear and arctangent fits to observations (red dots). Three regions labeled as 1, 2, and 3 represent the divergence zone, the weak convergence zone, and the strong convergence zone, respectively. Symbols, curves, and labels in the panel (b) are the same as in (a), but observations were taken from behind the propagating NLIWs.

II. INTERNAL WAVES IN THE VICINITY OF KUROSHIO PATH

OBJECTIVES

For this project, our broad focus was on inertial waves, internal tides, the internal wave continuum, and nonlinear internal waves in a complex and diverse dynamic environment (Fig. 13) where the Kuroshio interacts with the shallow and the deep topography (Tang et al., 2003), strong nonlinear internal waves and finescale inertial shear layers were observed (Rainville and Pinkel, 2004), and strong internal tides have been suggested by numerical models (Niwa and Hibiya, 2004). The primary objectives of this project were 1) to provide a geographical map and the long-term variation of internal wave energy and shear variances, 2) to quantify high-frequency nonlinear internal wave energy, 3) to quantify the energy and shear of inertial waves along the Kuroshio path, and 4) to identify generation sites of baroclinit tides in Luzon Strait, and quantify their energy flux and dissipation rates.

APPROACH

We analyzed observations taken in the vicinity of the Kuroshio path from the Luzon Strait to the southern East China Sea. Available data sets include 1) moored and bottom mounted ADCPs, and shipboard ADCP observations, 2) CTD profiles, 3) moored temperature, 4) moored current meter, and 5) echo sounder. Previous studies of these data focused primarily on sub-inertial processes. Most of available data were taken at a sampling rate of < 60 minutes, suitable for studying internal waves. We collaborated with Taiwanese investigator, performed numerical model simulation and analyzed model results of baroclinic tides in Luzon Strait.

WORK COMPLETED

- A preliminary analysis of historical CTD data was performed to quantify the seasonal variations of the Kuroshio front in the Luzon Strait and along the east coast of Taiwan.
- With Dr. Jan Sen we performed a numerical model simulation to investigate the energy budget of barotropic and baroclinic tides in the Luzon Strait (Jan et al., 2008). We identified the generation and dissipation sites of baroclinic tides and quantified the energy flux, the generation rate, and the dissipation of barotropic and baroclinic tides.

RESULTS

The water mass east of the Philippines is often defined as Kuroshio water (black block in Fig. 14), and the water mass west of the Philippines is often defined as South China Sea water (red block in Fig. 11) (Chern and Wang, 1998). Within the Kuroshio along the east coast of Taiwan, both types of water have been observed (Fig. 15). It is unclear where and how these two water masses mix. Within the Luzon Strait the Kuroshio, barotropic tides, baroclinic tides, and other oceanic processes interact with submarine ridges; they are potential sources for the turbulence mixing (Fig. 14).

Averaged density fields across the Kuroshio along the east coast of Taiwan in summer and in winter were constructed using historical CTD data collected by the National Center for Ocean Research (NCOR) between 1985 and 2002 (Figs. 16 and 17). The isopycnal tilts associated with the Kuroshio and the boundary countercurrent along the east coast of Taiwan are revealed. Similar temperature and salinity fields were constructed, as well as fields of their standard deviations (not shown).

The spatial and temporal variations of baroclinic tides in the Luzon Strait were investigated using a three-dimensional tide mode. Luzon Strait is the primary deep passage between the Pacific Ocean and the South China Sea (Figure 18). The Kuroshio and tides are the dominant currents in the Luzon Strait. The barotropic tidal currents oscillate at amplitudes of 0.05–0.3 m s^{-1} with major axes nearly perpendicular to the two ridges in the Luzon Strait such that strong baroclinic tides are generated. The double ridges cause strong dissipation of barotropic and baroclinic tidal energy. The energy budget is summarized in Figure 18b. On average, 30 GW of baroclinic tidal energy, including all four major tidal constituents, are generated within the Luzon Strait. About 6.6 GW of baroclinic tidal energy propagates into the South China Sea, and 5.6 GW of baroclinic tidal energy propagates into the Pacific Ocean. There is a loss of 18 GW of baroclinic tidal

energy within the Luzon Strait either via turbulence mixing or transformed into non-hydrostatic processes, e.g., nonlinear internal waves (NLIWs), which are not resolved by the model. Previous studies show the energy flux of NLIWs in the South China Sea is ~2 GW (Klymak et al., 2006). Assuming all the loss of baroclinic tidal energy is dissipated locally within the Luzon Strait, the average turbulence kinetic energy dissipation rate per unit mass, ε, within the Luzon Strait is $\sim 10^{-7}$ W kg^{-1}, and a bulk estimate of the vertical eddy diffusivity is $O(10^{-3})$ m^2 s^{-1}. The inferred turbulence kinetic energy dissipation rate and vertical eddy diffusivity are a factor of 100 greater than those in a typical open ocean suggesting strong turbulence mixing induced by breaking baroclinic tides.

Details of barotropic to baroclinic tidal energy conversion and energy fluxes for four individual tidal constituents are shown in Figure 19. Among the four tidal constituents, the S2 baroclinic tide is the weakest within the Luzon Strait. About 70% of baroclinic tidal energy is generated at the east ridge, and 30% is generated at the west ridge. The semidiurnal M_2 baroclinic tide propagates into the South China Sea and the Pacific Ocean in a narrow tidal beam, ~100 km.

The energy budget and the energy fluxes of baroclinic tides forced by the combined four major tidal constituent do not show significant seasonal variation. There is strong fortnightly variation (Figure 20). The baroclinic tidal energy generation, energy fluxes, and energy dissipation rates in the spring tide are about five times those in the neap tide.

REFERENCES

Chern, C.-S., J. Wang, The spreading of the South China Sea water to the east of Taiwan during summertime, *Acta Ocean.. Taiwanica*, **36**, 97-109, 1998.

Klymak, J. M., R. Pinkel, C.-T. Liu, A. K. Liu, and L. David, Prototypical solitons in the South China Sea, *Geophys. Res. Lett.*, **33**, L11607, doi:10.1029/2006GL025932, 2006.

Liang, W. D., T. Y. Tang, Y. J. Yang, M. T. Ko, and W. -S. Chuang, Upper-ocean currents around Taiwan, *Deep Sea Res.*, **40**, 1085-1105, 2003.

Niwa, Y. and T. Hibiya, Three-dimensional numerical simulation of the M2 internal tides in the East China Sea, *J. Geophys. Res., 109, C04027,* doi:10.1029/2003JC001923, 2004.

Rainville, L., and R. Pinkel, Observations of energetic high-wavenumber internal waves in the Kuroshio, *J. Phys. Oceanogr.*, **34**, 1495-1505, 2004.

Tang, T. Y., H. Y. Tai, and Y. J. Yang, The flow pattern north of Taiwan and the migration of the Kuroshio, *Cont. Shelf Res.*, **20**, 349-371, 2003.

PUBLICATIONS

Jan, S., R.-C. Lien, and C.-H. Ting, Numerical study of baroclinic tides in Luzon Strait, *J. Oceanogr.*, **64**, 789-802, 2008.

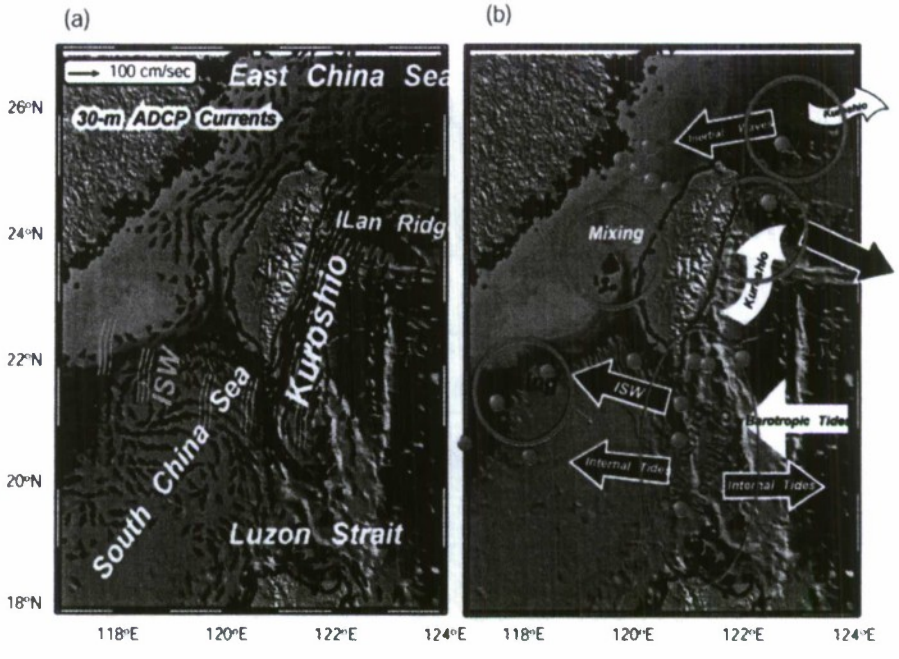

Figure 13: (a) Topography of western Pacific near Taiwan. Composite shipboard ADCP velocity at 30-m depth (figure adopted from Liang et al. 2003) shows Kuroshio crossing regions of strong topography in Luzon Strait and impinging on the continental shelf of the East China Sea northeast of Taiwan. (b) Potential small-scale processes in the region. Potential hot spots for generation of internal waves and turbulence mixing are red circled in (b). Red bullets mark positions of available mooring data for the present analysis.

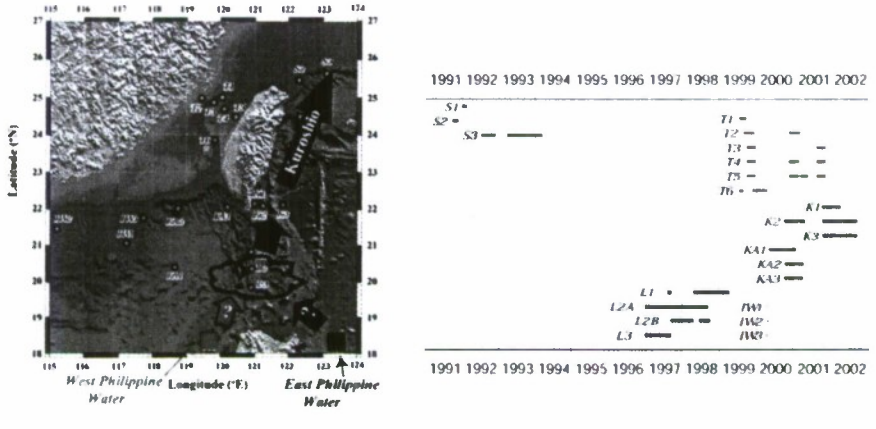

Figure 14: Positions (left panel) and periods (right panel) of moored ADCPs and current meters in East China Sea, Taiwan Strait, Kuroshio, Luzon Strait, and South China Sea. Stations of current meter and ADCP moorings are labeled. Red and black blocks represent the area where water masses are commonly defined as South China Sea water and Kuroshio water, respectively. We emphasize in our analysis that this definition is misleading and term them as west Philippine water and east Philippine water, respectively. In the main axis of the Kuroshio, e.g., station K2, the water mass is a mixture of these two water types.

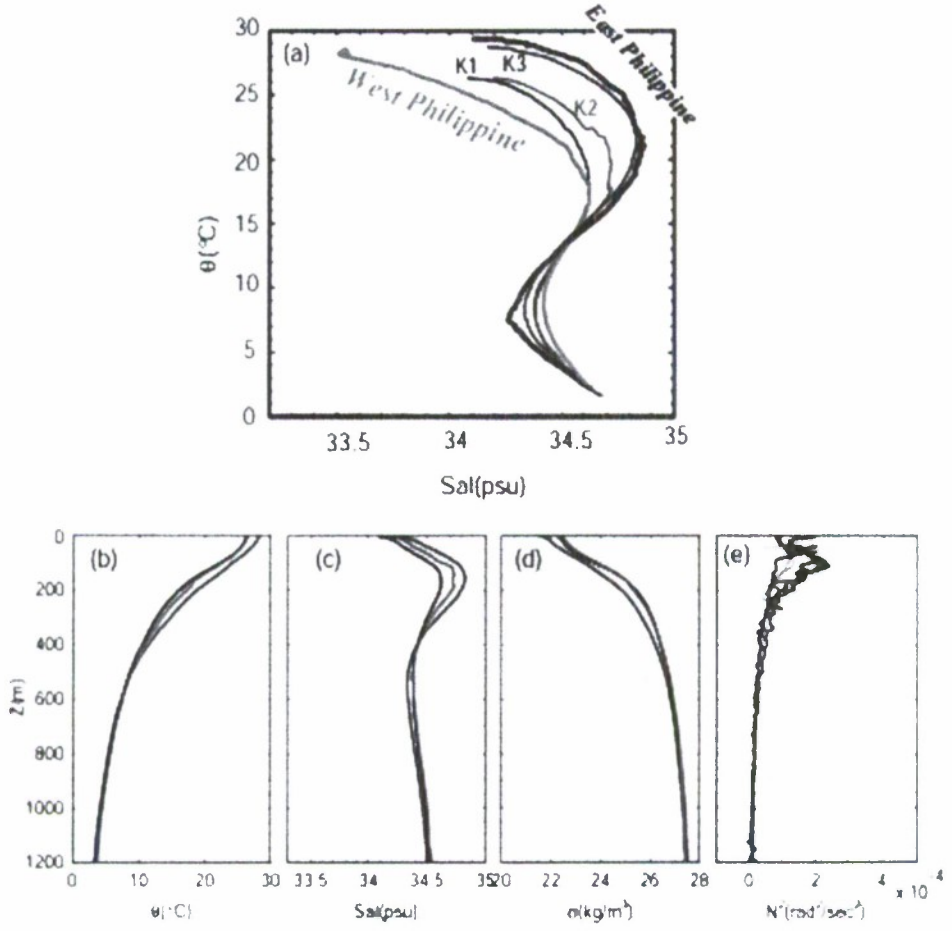

Figure 15: Water properties at three mooring positions, K1 (black), K2 (red), and K3 (blue). The panel (a) shows T-S properties of water masses at mooring stations, west Philippine water (magenta), and east Philippine water (thick black). Vertical profiles of potential temperature, salinity, potential density, and N^2 are shown in panels (b), (c), (d), and (e).Thin curves in panel (e) are total shear squared computed from mooring ADCP data.

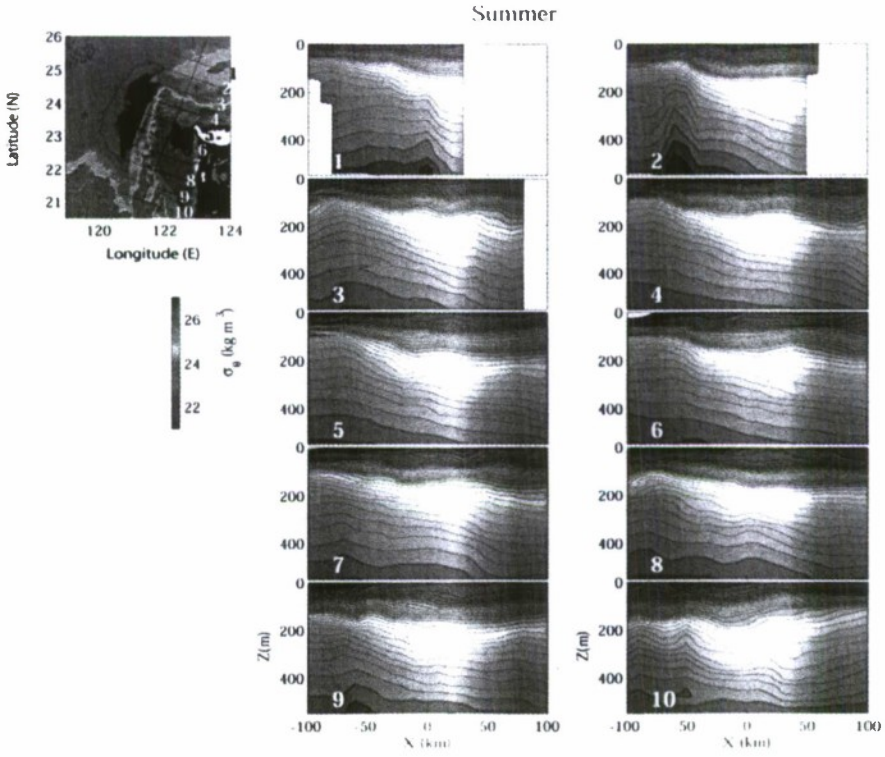

Figure 16: Average density fields in summer across the Kuroshio along the east coast of Taiwan constructed using historical CTD data.

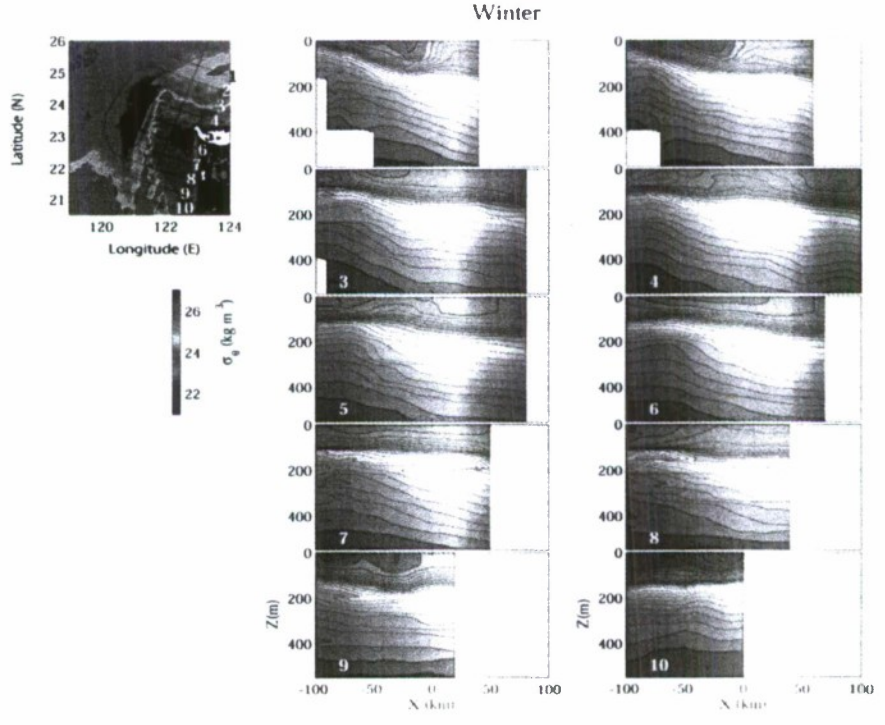

Figure 17: Average density fields in winter across the Kuroshio along the east coast of Taiwan constructed using historical CTD data.

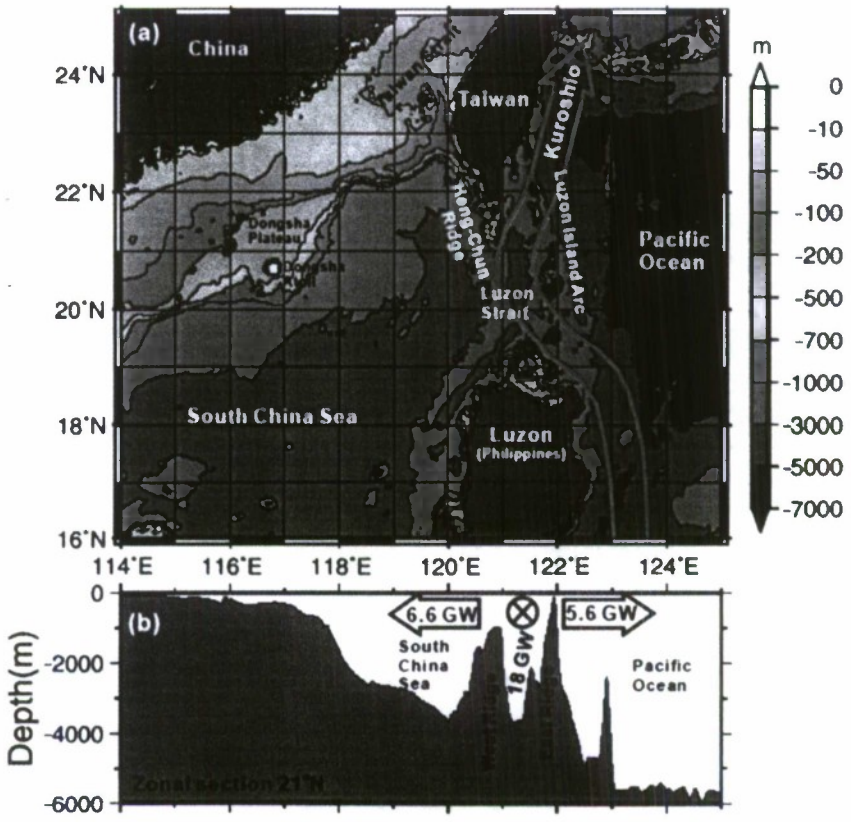

Figure 18: (a) Bathymetry in the northern South China Sea, northwest Pacific Ocean and Luzon Strait. (b) Topographic transect along 21°N and main results of baroclinic tidal energy fluxes and dissipation. Arrows of 6.6 and 5.6 GW represent the spring-neap mean baroclinic energy fluxes that propagate into the South China Sea and the Pacific Ocean, respectively, from the Luzon Strait. About 18 GW of the baroclinic tide dissipation occurs in the Luzon Strait. ⊗ marks the Kuroshio.

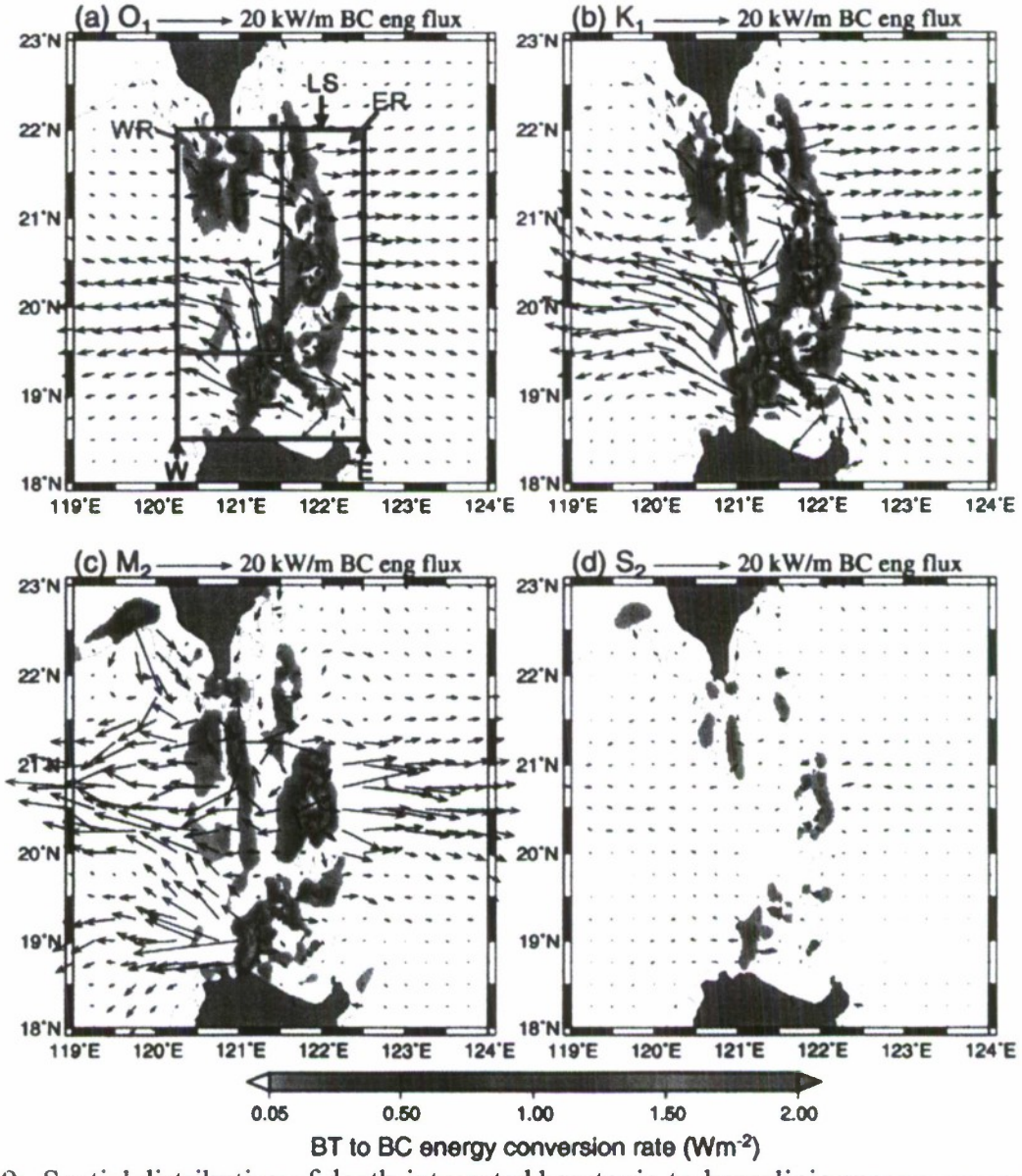

Figure 19: Spatial distribution of depth-integrated barotopic-to-baroclinic energy conversion rate (color shading) and baroclinic energy flux(vectors) for (a) O_1, (b) K1, (c) M_2, and (d) S_2 constitutents in summer. The black contour line represents the 1000-m isobath.

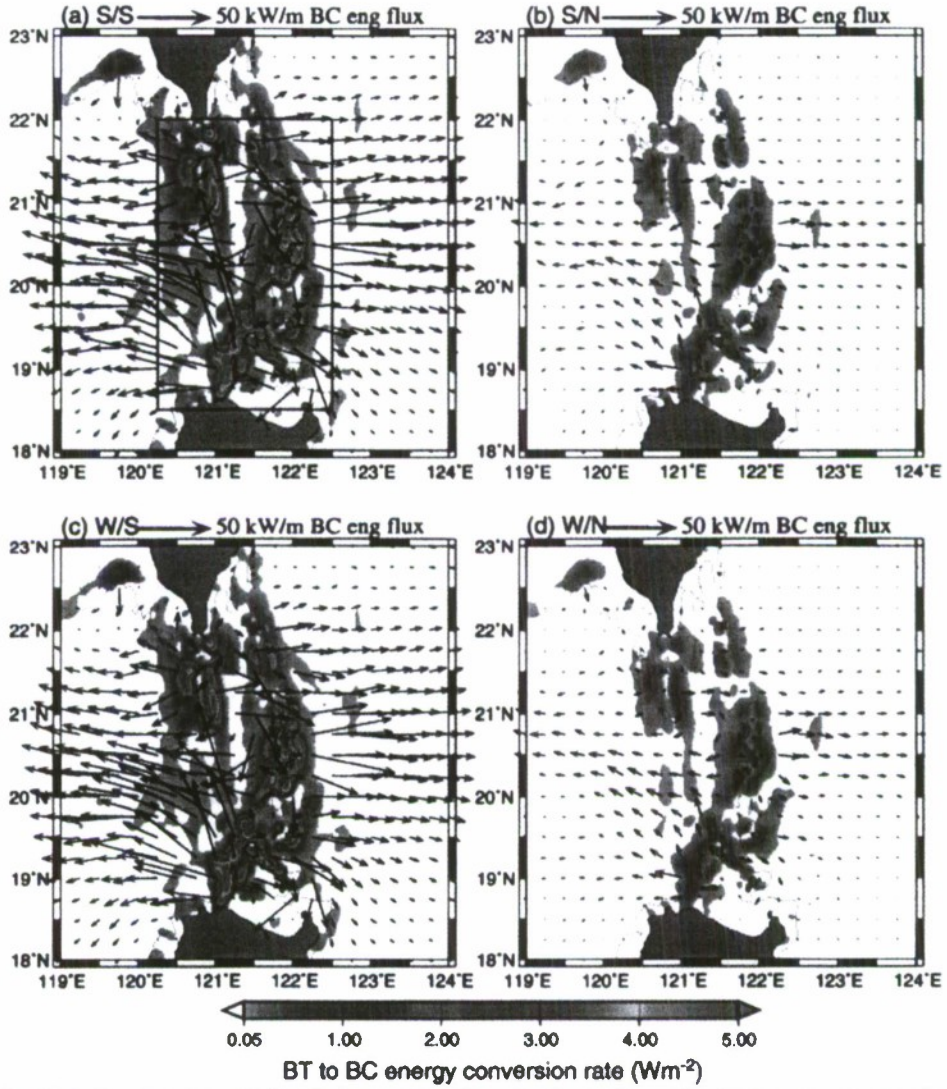

Figure 20: Spatial distribution of depth-integrated barotopic-to-baroclinic energy conversion rate (color shading) and baroclinic energy flux (vectors) for combined major tidal constituents O1, K1, M2, and S2 in (a) summer spring period, (b) summer neap period, (c) winter spring period, and (d) winter neap period. The black contour line represents the 1000-m isobath.